Carbon 135 (2018) 72–84

Contents lists available at ScienceDirect

Carbon

journal homepage: www.elsevier.com/locate/carbon

Development and properties of high thermal conductivity molybdenum carbide - graphite composites

Jorge Guardia-Valenzuela [a, b, *], Alessandro Bertarelli [a], Federico Carra [a, c], Nicola Mariani [d, 1], Stefano Bizzaro [e], Raul Arenal [b, f]

[a] CERN, CH - 1211, Geneva 23, Switzerland
[b] Advanced Microscopy Laboratory (LMA), Institute of Nanoscience of Aragon (INA), University of Zaragoza, 50018, Zaragoza, Spain
[c] Politecnico di Torino, Corso Duca degli Abruzzi 24, 10129, Torino, Italy
[d] ITER, Route de Vinon-sur-Verdon, CS 90 046 13067, St. Paul-lez-Durance, France
[e] Brevetti Bizz, Via dell'Industria - Loc. Tombole, Z.I. EST 3°, STRALCIO, I-37047 San Bonifacio, Verona, Italy
[f] ARAID Foundation, Zaragoza, 50004, Spain

ARTICLE INFO

Article history:
Received 26 January 2018
Received in revised form
24 March 2018
Accepted 5 April 2018
Available online 10 April 2018

ABSTRACT

A family of novel graphite-based composites reinforced with a dispersion of molybdenum carbide particles, with very high thermal and electrical properties, has been recently developed at CERN, in collaboration with Brevetti Bizz (IT), for applications in particle accelerators. These materials, produced by spark plasma sintering, assisted by liquid phase, have been extensively investigated and characterized. The influence of the initial constituents, together with the sintering parameters, have been studied in view of optimizing the thermo-physical and mechanical properties as well as ultra-high vacuum compatibility. The carbide phases and the microstructures have been analysed. Their excellent thermal conductivity (approaching 800 $Wm^{-1}K^{-1}$), low thermal expansion and low density make these materials appealing for high-end thermal management applications.

1. Introduction

Graphite has received great attention for nuclear applications since the first reactor was realised in 1944 [1]. Beyond the nuclear sector, many industrial applications extensively rely on graphite because it features extraordinary thermal and chemical stabilities, very low thermal expansion, while being a good electrical conductor.

In particle accelerators, such as the *Large Hadron Collider* (LHC) at CERN [2], graphitic materials are extensively adopted in *beam intercepting devices* (BID), which are designed to withstand the extreme conditions (temperatures and pressures) induced by the accidental or deliberate impact of particle beam pulses on matter. On top of ensuring outstanding thermal shock resistance, these materials must typically fulfil a number of additional requirements, such as high geometrical stability and resistance to radiation damage [3]; in some cases, as in collimators for circular accelerators, high electrical conductivity is also sought to limit their destabilizing effects on particle beams [4].

LHC collimators (Fig. 1a) are a family of BID relying on two movable girders, known as jaws (Fig. 1b), which interact with external particle halo to control size and shape of the particle beam and shield delicate accelerator components such as superconducting magnets from highly energetic particles [5]. In normal operation, only a tiny fraction of the beam is intercepted by the collimator jaws; however, this is enough to induce significant heat loads, which may grow up to 25 kW over several seconds [6]. High thermal conductivity is required in jaw materials to minimize temperature gradients which may lead to unacceptable thermal deformations, and to limit temperature peaks which may cause, inter alia, excessive outgassing rates.

Moreover, in case of accidental orbit errors, a direct impact of the proton beam on the jaw can occur, generating a rapid increase of temperature and pressure (thermal shock), potentially leading to the failure of the component [7] [8] [9].

The design of collimators presently installed in the LHC largely relies on graphite-based materials such as *Carbon Fibre-reinforced Carbon* (CFC) [5]. These materials have so far very well performed.

* Corresponding author. CERN, CH - 1211, Geneva 23, Switzerland.
E-mail address: jorge.guardia.valenzuela@cern.ch (J. Guardia-Valenzuela).
[1] Formerly at CERN and Politecnico di Milano, Italy.

https://doi.org/10.1016/j.carbon.2018.04.010

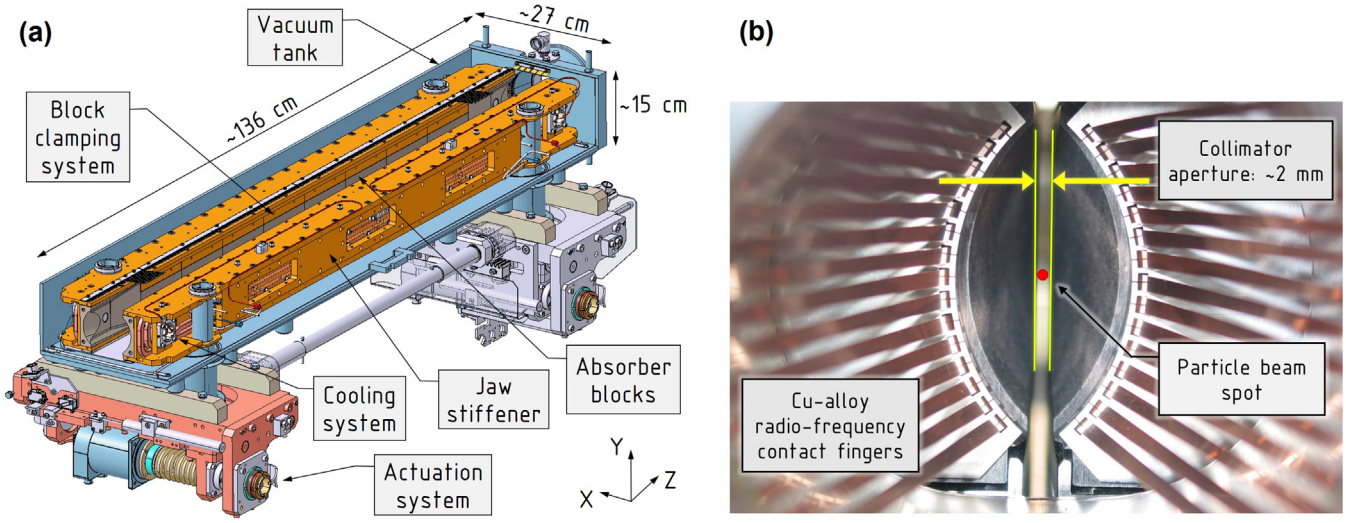

Fig. 1. (a) 3D sectioned CAD model of a HL-LHC collimator prototype (b) Front-view of an LHC collimator showing the size of jaw aperture in operation.

In the coming years, however, an important upgrade, known as *High Luminosity LHC* (HL-LHC), is foreseen, increasing the stored beam energy from 362 to 692 *MJ* [10]. This trend is set to continue in future studies such as the 80÷100 *km* long *Future Circular Collider* (FCC), with a projected stored energy of 8.4 GJ [11]. The loads in operation on collimators will consequently increase significantly.

None of the materials currently employed in the active part of LHC Collimator jaws is predicted to fulfil all the requirements posed by the more severe working conditions expected in the HL-LHC: in particular, numerical simulations indicate that the limited electrical conductivity of graphite and CFC may induce electro-magnetic instabilities in the particle beam [12]. Other graphite-based materials such as forms of *Highly Oriented Pyrolytic Graphite* (HOPG) have been considered. These materials have thermo-physical properties that exceed the requirements in the direction of the basal planes, however, they poor intrinsic performance in the through-plane direction make them unfit in the HL-LHC collimators. The uncommon combination of properties required can be met by certain graphite-matrix composites, particularly those including the advantages of *liquid phase* (LP) sintering.

One of the first published attempts at producing metal (carbide) – graphite composites sintered with metals in liquid form was that by Humenik and colleagues [13]. Graphitic materials produced by hot-working with a dispersed liquid carbide phase (termed HWLC) were firstly investigated by White and Pontelandolfo [14] [15] for the purpose of developing graphite-based materials with improved properties for high-temperature nuclear and aerospace applications. The observed strengthening effect with the HWLC method was in sharp contrast to bodies hot-worked in similar conditions but without the carbide additives, and to bodies including the carbide phase but hot-worked at temperature below carbide melting point [14]. The strengthening effect of the carbide inclusions was also demonstrated in Ref. [16], in comparison with bodies without the inclusions hot-worked in the same conditions (2700°*C*).

Although appreciable reductions in gas permeability and increase in strength were attained, the overall improvement was limited. R.B. Matthews [17] presented a very comprehensive study of the HWLC materials, comparing different additions, treatments and studying the strengthening mechanism in detail, especially the interactions between molten molybdenum carbide and carbon [18]. The R&D program presented in this paper has investigated novel materials based on this mechanism, while addressing some of the drawbacks and limitations of past attempts.

Apart from high densification through void infiltration, the LP induces catalytic graphitization by dissolution of individual carbon atoms, eventually connecting them to form solid graphite [19]. This continuous dynamic dissolution-precipitation process dissolves the most disordered and hence most reactive carbon structures – such as amorphous regions or edges of basal planes – and precipitates fresh graphite that grows and bonds together the initial graphite crystallites [17] [18] [20]. The existence of a decreasing solid solubility of carbon in $\alpha - MoC_{1-x}$, see Fig. 5, leading to precipitation of the excess carbon in the form of graphite also during cool down, might contribute to the high cohesion of the graphite matrix. However, other systems such as Ti-C or V-C, not exhibiting a decreasing solubility line, still exhibit significant strengthening [16].

If high temperatures are involved, the defects within the graphitic structure have high mobility, which progressively improves the lattice towards the ideal graphite crystalline structure (interplanar spacing $d_{002} = 0.3355\ nm$). This is the (standalone) graphitization process. Graphitization is a temperature-dependent process which begins at temperatures close to 2300 K. The strongest temperature-dependent structural changes by the graphitization process occur close to 2550 K, the so-called graphitization threshold which is the minimal heat treatment temperature for the development of true graphitic ordering [21]. For practical reasons, highly graphitized commercial products typically receive thermal treatments at temperatures above 3000 K to ensure the efficient development of the graphitic structure [22].

Catalytic graphitization modifies the process energetic pathways and allows production at lower temperatures with significantly shorter process durations. While the catalytic graphitization process is favoured by higher temperatures and longer sintering times, an optimal particle size of catalyst and carbon-based precursors as well as their homogeneous distribution are necessary to reach a satisfactory final material structure.

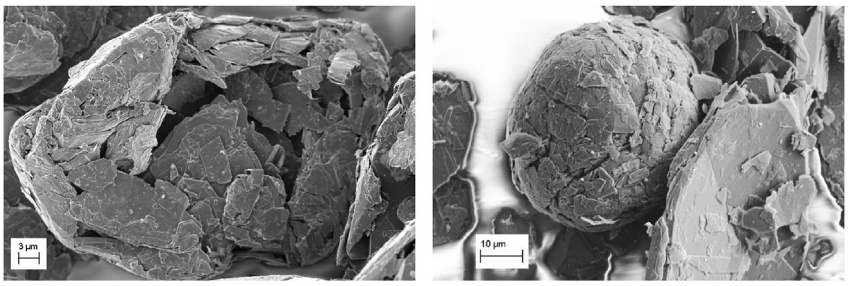

Fig. 2. Typical microstructure of the Asbury 3260 spheroidal-flake graphite powder.

In this context, a family of graphite-matrix composites reinforced with molybdenum carbides (Molybdenum Carbide – Graphite, *MoGr*) has been co-developed by CERN and the Italian SME Brevetti Bizz [23], partly within the EuCARD, EuCARD-2[2] and ARIES[3] collaborations, with the goal of increasing the electrical conductivity of collimator materials, while maintaining or improving the beam impact robustness of currently adopted CFC jaws [24].

A recent beam-impact experiment (HRMT-23) at the CERN HiRadMat facility [25] demonstrated the validity of the design of HL-LHC secondary collimator with MoGr absorbers [7] [26] [27]. A collimator prototype using this novel composite material has been manufactured and is being tested in the LHC ring.

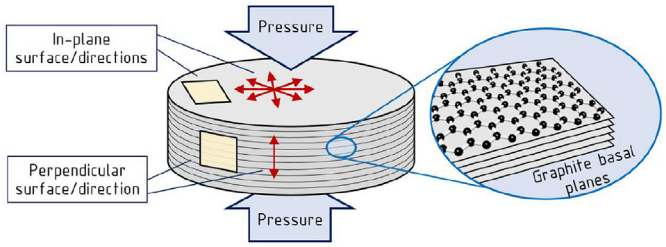

Fig. 3. Preferred orientation of graphite basal planes with respect to the applied uniaxial pressure. Naming convention for the material directions. (A colour version of this figure can be viewed online.)

2. Experimental

2.1. Production

MoGr is processed by *spark plasma sintering* (SPS), in the presence of LP, starting from powders of graphite, molybdenum and, in some grades, *carbon fibres* (CF) and titanium. SPS, a variation of hot-pressing, is a powder metallurgy technique that uses the flow of electrical current through the material and the mould as heating source.

The graphite powder used is grade 3260 from Asbury Carbons Company, consisting of crystalline natural graphite with spheroidal-flake morphology (Fig. 2), with a mean particle size of around 30 μm, and at least 90% of the particles between 10 and 80 μm. This morphology was chosen to limit the anisotropy of the final material, as well as to facilitate the compactness [24]. In contrast to examples of prior art based on carbon fillers and binder pitch as raw materials, already graphitized constituents are used, making carbonization and graphitization stages unnecessary. Molybdenum and titanium powders have a mean particle sizes of 5 μm, and metal purity higher than 99.9%. Pitch-based CFs are present in two grades, MG-6530Aa and MG-6541Aa, with a diameter of 10 μm and a length of 250 μm (Cytec ThermalGraph DKD) or 3 mm (NGF Granoc XN-100-03Z). The addition of CFs is a further difference with respect to prior art.

The powder mixture is prepared in a 3D mixing machine, dry and without any mixing media, and then compacted into a green body at up to 300 *MPa* in a uniaxial hydraulic press, inside a steel mould. Compression-induced shear stress preferentially orients the graphite grains with their basal plane perpendicular to the pressing direction (Fig. 3). Due to the spheroidal shape of the graphite powder, a minor part of the graphite grains is present in other-than-the preferred orientation. Even if CFs, when present, are dispersed randomly together with the other powders in the mixing machine, they likely have preferred orientation after compaction, with their axis perpendicular to the pressing direction. The green body is then inserted into a tailor made graphite mould consisting in top and bottom punches and a lateral container (Fig. 4); this is an additional difference with respect to the HWLC process developed by White and Pontelandolfo [15] where the lateral surface was free to expand and to allow the excess liquid to be squeezed out. John and Jenkins showed that hot-working radial strain is beneficial for strengthening, up to a certain extent when cracks appear and lower the properties [16]. The sintering cycles are performed in a current-assisted sintering machine custom-built by Brevetti Bizz, capable to reach sintering temperatures in excess of 2700 $^{\circ}C$, while applying a pressure of up to 35 *MPa*. It is well known that the application of pressure thermodynamically favours graphitization [28]: sintering pressures are limited by the mechanical strength of the mould. The direct current through the electrode is typically around 15 *kA* for plates with area of 150 cm^2 ($\sim 100\ A\ cm^{-2}$), which produces a power loss in the order of 100 *kW*. The morphology of the components and the manufacturing process lead to a transversely

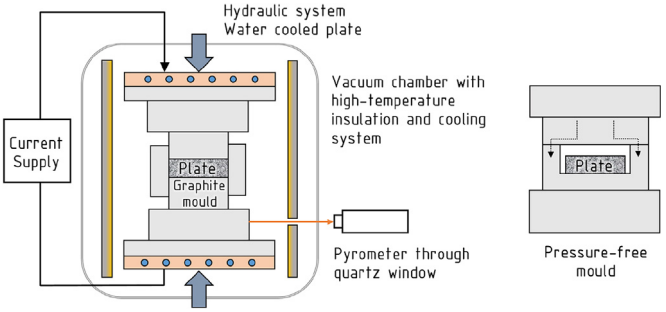

Fig. 4. Schematic of the sintering machine used. Once sintered, the pressure-free mould is used for the post-sintering cycle. (A colour version of this figure can be viewed online.)

[2] http://eucard2.web.cern.ch/.
[3] http://aries.web.cern.ch/

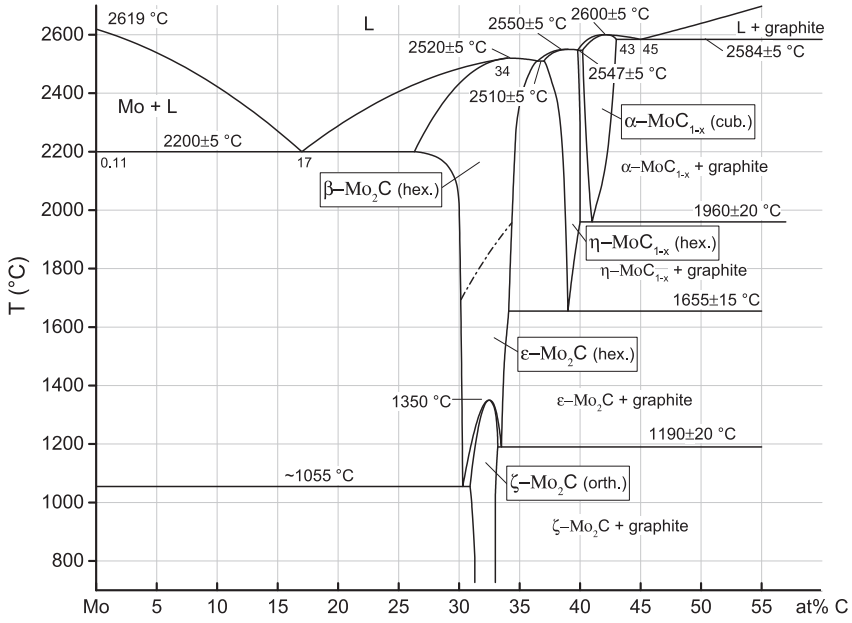

Fig. 5. Mo-C phase diagram [29].

isotropic material: the in-plane and perpendicular directions are defined as those parallel and perpendicular to the graphite basal planes, as shown in Fig. 3.

The sintering temperature exceeds the eutectic temperature of molybdenum with carbon ($2584^{\circ}C$), forming a LP containing large amounts of dissolved carbon; the eutectic molybdenum-carbon contains 45 *at.%* of carbon (Fig. 5).

Since, during sintering, part of the LP flows out of the plate impregnating the graphite mould, the final composition results in a lower carbide content compared to the theoretical one, based on initial Mo content. This entails difficulties to calculate the actual compaction and the final composition, because the exact measurement of the amount of LP spill is not practicable.

The processing temperature is controlled by means of an optical pyrometer; in the sintering set-up used, the temperature is read on the lower punch, to limit issues related to the very high temperatures achieved (Fig. 4). Since a non-negligible temperature gradient exists between the measuring point and the core, the actual temperature during the process can be inferred by recording the temperature at the moment of the eutectic reaction ($2584^{\circ}C$), which can be deduced by the change in compression speed due to ongoing melting. The presence of molten material squeezed out of the plates confirms that the eutectic point is reached.

After sintering, the plate is submitted to a pressure-free heat treatment aiming at releasing the internal stresses induced by the sintering cycle. This is performed inside a special set-up allowing the flow of current through the mould walls without the application of pressure to the plate.

The size of the final plates can be 100×150 *mm*, with a thickness of around 30 *mm*. Out of these, specimens for the characterization as well as full-size collimator blocks have been machined, hence ushering in industrial-scale production. Other shapes, such as discs, are also possible.

Gas pressure inside the sintering machine is lower than $\sim 10^{-1}$ *mbar*. Due to the closed geometry of the moulds during sintering, the effect of the chamber pressure in material gas content might be negligible. On the other hand, the pressure-free set-up used for the post-sintering heat treatment includes openings in the mould, allowing material outgassing and improving pumping.

Out of the 15 different grades produced and characterized at CERN [24], focus is given to the four most recent which benefit from better knowledge of the detail of the production process (Table 1). Unfortunately, the number of tests, to evaluate the influence of individual variables, was limited by reason of time. The testing combinations were chosen to maximize the probability of success in the final properties. The four MoGr grades presented in this study are shown in Table 1. The initial composition is reported, as well as the parameters of the sintering and the post-sintering cycles. The digits of the identifier depend on the initial content of molybdenum, graphite, carbon fibres and titanium powders respectively. The final letter tag the different post-sintering treatments. The relevant differences between each grade and the previous one are in bold. The main variables are the content of titanium, CF, and the temperature of the post-sintering cycle.

2.2. Characterization

After production, samples for thermomechanical characterization were machined by conventional milling methods from the sintered plates. For measuring each property, three samples per direction were tested and the resulting values averaged. In temperature dependent plots, the curve shown corresponds to the best fit of all measurements.

The thermomechanical characterization was performed at CERN, with the following equipment: Netzsch *Differential Scanning Calorimeter* (DSC) Pegasus 404C, Netzsch *Laser Flash Apparatus* (LFA) LFA427, Archimedes scale, Netzsch horizontal pushrod dilatometer DIL 402E, and Zwick/Roell Z400 Universal Testing Machine. Full details of the measurements can be found in Ref. [30] [31] [32]. The accuracy of these measurements is within 5%.

All the shown density values are calculated from the apparent solid volume measured with the Archimedes Scale, therefore including closed porosity.

The bending strength was measured according to the standard ASTM C1161-02, with the 4 point configuration. Strains were measured with a strain gauge glued to the face under tensile stress.

Table 1
Initial production parameters of the four grades presented.

	MG-6530Aa		MG-6541Aa		MG-6403Ga		MG-6403Fc	
Vol.% Molybdenum	4.5		4.4		4.5		4.5	
Vol.% Graphite	90.5		90.1		**94.95**		94.95	
Vol.% Short CF[a]	0		**5**		**0**		0	
Vol.% Long CF[a]	5		**0**		0		0	
Vol.% Titanium	0		**0.5**		0.55		0.55	
	S	PS	S	PS	S	PS	S	PS
Estimated temperature ($^{\circ}C$)	$\sim$ 2600	$\sim$ 2100	$\sim$ 2600	$\sim$ 2100	$\sim$ 2600	$\sim$ 2100	$\sim$ 2600	$\sim$ 2600
Time (s)	2400	3000	2400	3000	2400	3000	2400	3000
Pressure on the plate (MPa)	35	0	35	0	35	0	35	0

Sintering cycle (S), Post-Sintering thermal treatment (PS).
[a] Short carbon fibres: length of 250 μm, long carbon fibres: 3 mm.

The elastic constants were computed from the resonance frequencies of parallelepiped samples, measured in the two different orientations of the material with the *impact excitation technique* (IET) according to standard ASTM C1259-01. As the standard method was not devised for anisotropic materials, such as MoGr, the measured frequencies were used as inputs in a finite element analysis optimization algorithm (ANSYS), described in Ref. [33].

The thermal diffusivity was measured according to the flash method ASTM E2585. The thickness of the usual LFA samples ($Ø10 \times 2\ mm$) was detected to be problematic even when using the shortest practical laser pulses (0.6 ms), because the characteristic diffusion time is of the same order of magnitude. This effect was observed when measuring samples of different thicknesses from the same material, in the in-plane direction and at low temperatures (high diffusivity). Thicknesses between $5-10\ mm$ were observed to provide more accurate results, and were adopted for the in-plane diffusivity measurements presented in this paper.

The electrical conductivity of parallelepiped specimens is calculated out of their dimensions and of their resistance, which is measured using four-wire sensing in order to eliminate electrode-specimen contact resistance from the measurement. The set-up is analogous to that proposed by the standard ASTM C611-98. In the in-plane direction, an eddy-current commercial device *Sigmatest 2.069* from Foerster (in the full frequency range $60-960\ kHz$) gives electrical conductivity values within ±10% with respect to the method aforementioned. Due to the anisotropy of MoGr, in the perpendicular direction, the device measures a sort of 3D-bulk average, thus resulting not appropriate for this direction. In-plane values both from four-wire and eddy-current methods are shown in Table 5.

Microstructural analyses were performed using a Zeiss Sigma field emission *scanning electron microscope* (SEM). Samples prepared for SEM observation were progressively polished with silicon carbide polishing discs under water flow (up to grit size P1200), to continue with diamond polishing paste on polishing soft cloth. Last step applied was using 1 μm diamond paste. Ion-polishing was performed with a Gatan Ilion II argon milling system.

X-ray diffraction (XRD) analyses were performed with Siemens D5000 diffractometer with Bragg-Brentano $\theta-2\theta$ configuration, using Cu $K-\alpha_1$ radiation ($\lambda = 1.54056$ Å) at *room temperature* (RT). Lattice parameters of the carbide phases were obtained from Rietveld refinement using *Materials Analysis Using Diffraction* (MAUD) software. If the crystallites in the sample are smaller than 500 nm, the diffraction conditions are not ideal and the peaks become broadened. An analysis of diffraction peak broadening can be used to determine the crystallite sizes up to 500 nm [34]. Rietveld refinement was also used to obtain the graphite crystallite size after calibration of the instrumental broadening with a LaB_6 powder reference sample. The broadening effects considered (Delft model) were the crystallite size and the instrumental broadening, and the refinement was performed with "arbitrary texture" and "anisotropic crystallite size" model. The surface state of the samples for XRD analyses was as-received from the supplier. No relevant differences in the position of the diffraction peaks were found by changing the surface state, for instance after polishing or ultrasonic bath cleaning. In order to improve the readability of the graphs, all XRD analyses were performed on perpendicular surfaces, in this manner the most intense peaks of graphite, mainly the (002) and (004), had reduced intensity due to the texture. Besides that, this orientation favours the diffraction of the set of planes (100) and (110), which allows to obtain the basal plane crystallite size (L_a). The texture of the carbides and of the graphite matrix is being investigated and is not covered in this article.

3. Results

3.1. Microstructural characterization

Fig. 6 shows SEM observations of polished MG-6541Aa in-plane and perpendicular surfaces. The as-polished surfaces show a connected graphite matrix (dark) with molybdenum carbide particles (bright) having an average size of 5 μm. The average number of particles per unit area is around $5 \times 10^3\ p\ mm^{-2}$ which corresponds approximately to $1 \times 10^6\ p\ mm^{-3}$. In Fig. 6(c) and (d) it is possible to appreciate how the carbides tend to elongate in the direction orthogonal to the force (pressing force was vertical on Fig. 6(c) and (d)), filling the voids between graphite flakes. The images show good compaction. Image analysis of ion-polished surfaces shows less than 0.5% of volume of voids (Fig. 7). The microstructures show no relevant changes between the different grades.

The homogeneity of the microstructure is confirmed by the repeatability of the thermo-mechanical measurements in samples obtained from different positions of the plate.

Differences in light reflectivity and/or scattering of the polished samples were observed in the two different orientations of the material after applying the same polishing process (Fig. 8). The preferred orientation of the graphite matrix allows flatter surfaces perpendicular to graphite basal planes compared with in-plane surfaces.

Both polished surfaces were also submitted to ultrasonic bath in ethanol at RT during 15 min. Sonication is an efficient method to remove dust from the surface prior to microscopical observations, but this treatment was found to change the visual appearance of MoGr, especially in one of the two orientations. The quality of the mirror surface was worsened after sonication, in particular in the in-plane surfaces.

Some of the graphite flakes were removed from the surface during the ultrasonic bath. On perpendicular surfaces, the removal is much less severe. Due to its anisotropic sp^2 hybridization, C-C bond in graphite is much weaker between basal planes than inside them ($7\ kJ/mol$ and $524\ kJ/mol$ respectively [22]), resulting in an

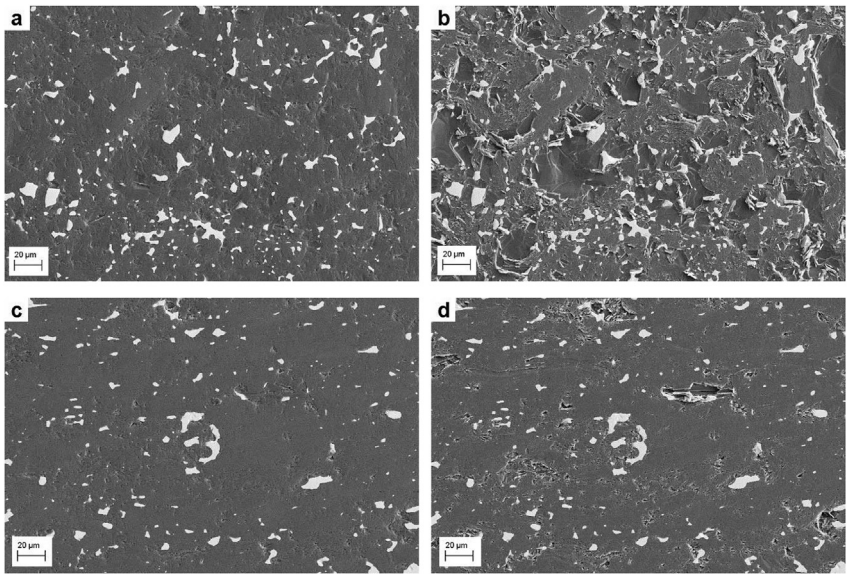

Fig. 6. SEM polished in-plane surface before (a) and after ultrasonic bath (b). Polished perpendicular surface before (c) and after ultrasonic bath (d). All micrographs corresponding to MG-6541Aa grade.

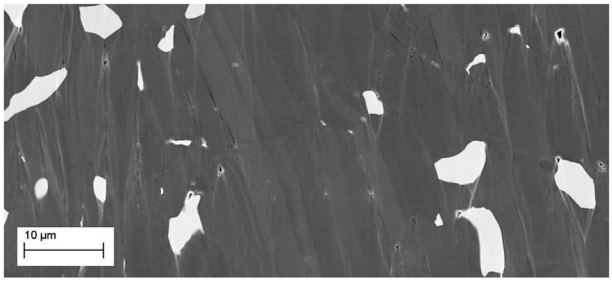

Fig. 7. Perpendicular ion-polished surface of MG-6403Fc. The graphitic planes are oriented vertically in the image.

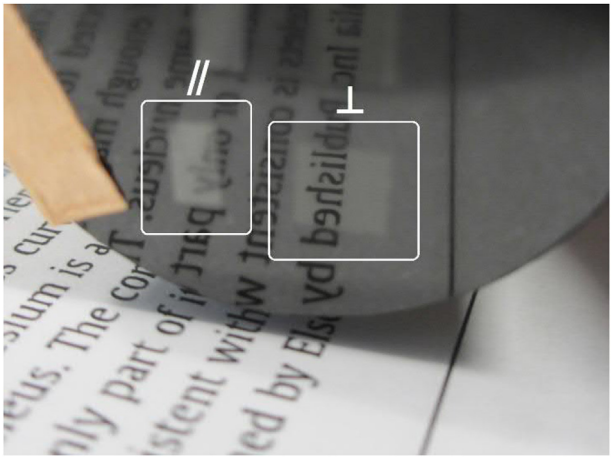

Fig. 8. Molybdenum graphite samples embedded in a black resin cylinder and polished for SEM observation, showing differences in light reflectivity/scattering between in-plane and perpendicular surfaces. (A colour version of this figure can be viewed online.)

easier removal of flakes attached only to basal-plane surfaces. Furthermore, carbides can only form a strong bond with the edges of graphite planes [18]. These effects allow weakly bonded graphite flakes to be removed by ultrasonic bath if they are exposed at the surface. Since not all graphite flakes stay in the preferred orientation, there are intact zones of in-plane surfaces after sonication and, conversely, removal of some particles in the perpendicular surfaces.

Energy-dispersive X-ray spectroscopy (EDS) analysis was performed in the finished materials, the results are shown in Table 2 together with the calculated initial composition. The total C values correspond to the sum of carbon from graphite and from the carbides. The final values presented are corrected to account for the EDS interaction volume in the graphite matrix higher than in the carbide phases; if no correction is applied, the carbon content is overestimated.

The four grades show a reduction in the metallic content, due to the loss of LP with composition close to the eutectic liquid. This effect is slightly more acute in the grades containing titanium, possibly related to the higher mobility of the LP when including the Ti doping. It is possible to see that molybdenum and titanium remain in the initial proportion, as shown by the Mo/Ti ratio.

3.2. X-ray diffraction analyses

Fig. 10 shows the comparison of the XRD measurements of the 4 grades. The intensities are normalized to (110) reflection of graphite, the intensity of the overlapping (222) reflection of the $\alpha - MoC_{1-x}$ phase is assumed to be negligible. The lattice parameters of the detected carbide phases are shown in Table 3. It is well known that cell dimensions of interstitial carbide phases can vary depending on the carbon content, the small deviations with the literature values could be due to either this effect or to XRD experimental errors.

All grades show graphite peaks corresponding to very high levels of graphitization, matching the positions of the ideal graphite structure ($a = 2.4617$ Å and $c = 6.7106$ Å [35]). The XRD comparison shows interesting results concerning the carbides. Apart from graphite peaks, grade MG-6530Aa containing no titanium shows multiple peaks matching those of dimolybdenum carbide Mo_2C and of hexagonal $\eta - MoC_{1-x}$ phases. According to the phase

Table 2
Initial and final chemical composition.

	MG-6530Aa		MG-6541Aa		MG-6403Ga		MG-6403Fc	
	Initial	Final	Initial	Final	Initial	Final	Initial	Final
Wt. % Total C	82.4	85.9	81.9	86.6	81.6	87.1	81.6	87.2
Wt. % Mo	17.6	14.1	17.2	12.7	17.5	12.2	17.5	12.1
Wt. % Ti	0	0	0.9	0.7	0.9	0.7	0.9	0.7
(Mo + Ti) *Wt.* % loss	20		26		30		30	
At. % Total C	97.4	98.0	97.1	98.0	97.1	98.1	97.1	98.1
At. % Mo	2.6	2.0	2.6	1.8	2.6	1.7	2.6	1.7
At. % Ti	0	0	0.3	0.2	0.3	0.2	0.3	0.2
Atomic ratio Mo/Ti	∞	∞	~ 9	~ 9	~ 9	~ 9	~ 9	~ 9

Table 3
Details of the detected carbide phases and TiC.

	Structure	Lattice parameters (Å) Literature	Lattice parameters (Å) This work	Density ($g\ cm^{-3}$)	CTE ($10^{-6}\ K^{-1}$)
$\zeta - Mo_2C$	Orthorhombic	$a = 4.735$	$a = 4.739$ [a]		9.1 (a)
		$b = 6.025$	$b = 6.022$ [a]	9.10	4.3 (b)
		$c = 5.210$[37]	$c = 5.215$ [a]		6.1 (c) [37]
$\zeta - Mo_2C$	Hexagonal[b]	–	$a = 3.011$		
	(Mo sublattice)		$c = 4.739$	–	–
$\eta - MoC_{1-x}$	Hexagonal	$a = 3.018$	$a = 3.008$		5.95 (a)
		$c = 14.63$[29]	$c = 14.61$	9.39	11.5 (c) [17]
$\alpha - MoC_{1-x}$	Cubic	$a = 4.266$[29]	$a = 4.264$	8.92[c], 8.52[d]	–
TiC	Cubic	$a = 4.328$[40]	Not detected	4.91	7.4 [40]

[a] Calculated from hexagonal molybdenum sublattice parameters. See section 3.2.
[b] See section 3.2.
[c] Calculated with a = 4.266 Å, $Mo_{0.59}C_{0.41}$ (see Fig. 5).
[d] Calculated with a = 4.264 Å, atomic ratio Mo/Ti = 9: $Mo_{0.531}Ti_{0.059}C_{0.41}$ (see Table 2).

diagram, the hexagonal $\eta - MoC_{1-x}$ is only stable above $1655^{\circ}C$, while here it is found at RT; this was also observed by Matthews [17] and was explained by that phase being easily retained during furnace cooling. Dimolybdenum carbide Mo_2C phase suffers a transition between the orthorhombic $\zeta - Fe_2N - type$ "low temperature" phase and the hexagonal $\varepsilon - Fe_2N - type$ based "middle temperature" phase at $\sim 1350^{\circ}C$, and then an order-disorder transition into a $L'3 - type$ structure at around $\sim 1960^{\circ}C$ [36] [37]. Due to the negligible X-ray scattering factor of carbon compared with molybdenum, the orthorhombic $\zeta - Mo_2C$ phase shows only peaks from the hexagonal partial structure of the molybdenum atoms. Parthé and Sadagopan [38] showed that neutron diffraction is a more appropriate technique for the Mo_2C phase identification. The relationship between the orthorhombic structure and the hexagonal molybdenum sublattice is given by: $a_{orth} = c_{hex}$, $b_{orth} = 2 \cdot a_{hex}$ and $c_{orth} = \sqrt{3} \cdot a_{hex}$. The detected dimolybdenum carbide Mo_2C phase is referred in Table 3 as orthorhombic $\zeta - Mo_2C$, but Fig. 10 shows only the peaks corresponding to its hexagonal molybdenum partial structure.

The *face centred cubic* (FCC) $\alpha - MoC_{1-x}$ phase is not stable under $1960^{\circ}C$ (Fig. 5). Small additions of elements with affinity for carbon higher than molybdenum, such as hafnium and boron, stabilize the FCC $\alpha - MoC_{1-x}$ carbide [39]. The small quantity of added titanium, as seen in the XRD results, is also stabilizing the FCC $\alpha - MoC_{1-x}$ phase. Grades MG-6541Aa and MG-6403Ga containing titanium show only the FCC phase $\alpha - MoC_{1-x}$ stabilized at RT. Grade MG-6403Fc shows also a very small peak corresponding to the most intense peak (101) of $\eta - MoC_{1-x}$ hexagonal carbide; as the only difference between grades MG-6403Ga and MG-6403Fc is the change in post-sintering treatment temperature, a possibility is a slight change in the cooling rate, which reduced the stabilizing effect of the titanium. Energy-dispersive X-ray spectroscopy (EDS) analysis performed with SEM confirms that the titanium is present only inside the carbide particles and not inside the graphite matrix.

The results of diffraction domain size (crystallite size) from the different samples produced, including the initial Asbury 3260 graphite powder (3 different samples), are presented in Table 4. For comparison purposes, a commercial material *Thermal Pyrolytic Graphite* (TPG) produced by Momentive (US) has been characterized at CERN. TPG is a form of HOPG produced by thermal decomposition of hydrocarbon gas, available in sizes compatible with collimators. The values shown correspond to the set of planes (110), which relates to the crystallite size along the basal plane of graphite (L_a). The details of the method are described in section 2.2.

Table 4
In-plane crystallite size (L_a) obtained by XRD Rietveld refinement (nm).

Asbury 3260	MG-6530Aa	MG-6541Aa	MG-6403Ga	MG-6403Fc	TPG
110±10	240	310	260	320	290

The relative increase of crystallite size from the initial Asbury graphite (110 *nm*) to the sintered MoGr materials (240 – 320 *nm*) confirms graphitization happening. While the difference in size between the MoGr grades is not significant, the trend follows that of their respective thermal and electrical conductivities, as seen in Table 5. On the other hand, higher values of crystallite size would have been expected for TPG material, as seen in conductivity values that are more than twice of MoGr in the basal-plane direction, see section 3.3. It is expected that the size of the grains, inversely proportional to the population of grain boundaries, has more influence in the transport properties than the size of the crystallites within the grains. Other methods to assess the actual size of the graphite grains such as *Electron Backscatter Diffraction* (EBSD) are being investigated.

3.3. Thermo-mechanical characterization

Thermo-mechanical characterization results are presented in Table 5 and Figs. 11 and 12. The properties of MoGr show a

transversely isotropic behaviour typical of oriented graphites, due to the stronger interatomic bond in the in-plane direction. The in-plane properties are those typical of a highly graphitized matrix, i.e. very high thermal and electrical conductivities, low *coefficient of thermal expansion* (CTE), good mechanical strength. Density values are in all cases very similar and close to 2.5 $g\ cm^{-3}$, just slightly higher than TPG (2.25 $g\ cm^{-3}$).

The electrical conductivity in the in-plane direction is approximately 1 $MS\ m^{-1}$ (resistivity 1 $\mu\Omega\ m$). Grade MG-6530Aa, which shows the lowest in-plane electrical conductivity, is the only one without titanium. Compared with other graphite-based materials, MoGr has in-plane electrical conductivity about 10 times higher than high-quality isotropic graphite. On the other hand, TPG showed in-plane values up to 2.4 $MS\ m^{-1}$ (resistivity 0.41 $\mu\Omega\ m$). The main contributor to the observed values can only be the graphite matrix because of the small volumetric content of isolated carbide inclusions, which in any case have a conductivity not higher than 2.0 $MS\ m^{-1}$ [41]. Thanks to the catalytic effect of the metal-carbon LP, the initial graphite flakes are bonded together in a highly oriented matrix, resulting in high electrical conductivity. *Thermal conductivity* (TC) approximately follows the trend of the electrical conductivity, with in-plane values at RT approaching 800 $W\ m^{-1}K^{-1}$; in TPG, the in-plane TC is 1685 $m^{-1}K^{-1}$. Fig. 11 shows the TC in the two directions and the specific heat. As graphite TC is dominated by phonon conduction, phonon thermal scattering reduces the TC when increasing the temperature. For this reason there is a sharp decrease from RT to around 300 $^{\circ}C$. The material still has a TC higher than 500 $W\ m^{-1}K^{-1}$ at 125 $^{\circ}C$, a typical maximum operating temperature for electronic devices. On the other hand, in the perpendicular direction, the TC is 55 $W\ m^{-1}K^{-1}$ at RT. This is still a significant improvement compared with TPG (8 $W\ m^{-1}K^{-1}$ in the perpendicular direction). The perpendicular electrical conductivity is around 0.07 $MS\ m^{-1}$ (resistivity 14 $\mu\Omega\ m$), compared with 0.0009 $MS\ m^{-1}$ (resistivity 1098 $\mu\Omega\ m$) in TPG.

The bending strength is about 75 *MPa* in the in-plane direction and 12 *MPa* in the transverse, except for grade MG-6403Fc, where it is 20% lower. The mechanical resistance is one of the biggest drawbacks of TPG, corresponding to 25.5 *MPa* in the in-plane direction (the perpendicular measurement is not available, but is expected to be negligible due to the weak π bond in graphite).

The secant CTE plotted in Fig. 12 represents the average value in each of the 4 selected ranges of temperature. The in-plane CTE is rather constant in temperature, as opposite to the perpendicular direction, which increases with temperature. The CTE 20–200 $^{\circ}C$ is around $2.2 \times 10^{-6}\ K^{-1}$ in the in-plane direction, except in the grade without titanium where it is a bit lower, and in the grade MG-6403Fc with high temperature treatment which exhibits a slightly higher value. In the perpendicular direction the trend is reversed, with an average value around $8 \times 10^{-6}\ K^{-1}$ for MG-6403Fc, pointing to a lower degree of anisotropy in this grade. TPG has a much higher degree of anisotropy, with an in-plane CTE of $-1 \times 10^{-6}\ K^{-1}$ and $34 \times 10^{-6}\ K^{-1}$ perpendicularly.

Material properties such as bending strength suggest a strong carbide-graphite bond, which not only bridges the original graphite powders along the in-plane direction, but also limits the basal plane slip (shear) and delamination since carbide particles connect edges of graphite particles on several layers [16] [17], see Fig. 9, significantly improving the strength and the transport properties and reducing the CTE in the perpendicular direction with respect to a highly oriented graphite. While TPG features excellent in-plane thermal and electrical conductivities compared with MoGr, its poor properties in the perpendicular direction hinder its use in HL-LHC collimators.

The residual deformation displayed in Table 5 represents the change in length after a thermal cycle 20 – 1900 – 20 $^{\circ}C$, typical of a dilatometry measurement, and provides an indication for the internal stresses of the material, generated by the sintering cycle. The measurements show that the material is always more stable in the in-plane than in the perpendicular direction, and the improvement in dimensional stability is proportional to the temperature of the post-sintering treatment.

Thermal diffusivity and CTE are measured from 20 to 1900 $^{\circ}C$ in inert atmosphere; repeated measurements on the same sample provide the same results, showing that the material is resistant to

Fig. 9. SEM close-look of a fracture surface perpendicular to graphite basal planes. Grade MG-6541Aa. Image shows the edge of a graphite flake with two bonded carbide particles.

Table 5
Thermo-mechanical characterization results at room temperature.

Direction[a]	MG-6530Aa		MG-6541Aa		MG-6403Ga		MG-6403Fc	
	∥	⊥	∥	⊥	∥	⊥	∥	⊥
Density ($g\ cm^{-3}$)	2.51		2.49		2.49		2.55	
Spec. heat ($J\ g^{-1}K^{-1}$)	0.60		0.64		0.60		0.62	
Elec. cond. ($MS\ m^{-1}$)	0.82	0.05	0.98	0.06	0.88	0.08	0.95	0.07
	0.88[b]		1.01[b]		0.93[b]		1.01[b]	
Th. diffus. ($mm^2\ s^{-1}$)	469	31	490	28	430	37	466	31
Th. cond. ($W\ m^{-1}K^{-1}$)	706	47	781	45	647	56	740	50
CTE $RT - 200^{\circ}C$ ($10^{-6}\ K^{-1}$)	1.7	11.6	2.3	10.0	2.0	9.3	2.7	7.9
Residual deformation (%)	0.04	0.17	0.02	0.14	0.02	0.18	0.00	0.12
Bending strength (*MPa*)	70.9±3	12±0	79.5±4	12.4±1	73.5±7	11.6±0	58.1±8	10±1
Elastic modulus (*GPa*)	76.7	4.7	85.8	4.5	74.2	3.8	60.4	4.0

[a] In-plane (∥) and perpendicular (⊥) directions, see Fig. 3.
[b] By eddy-current method, otherwise by four-wire method.

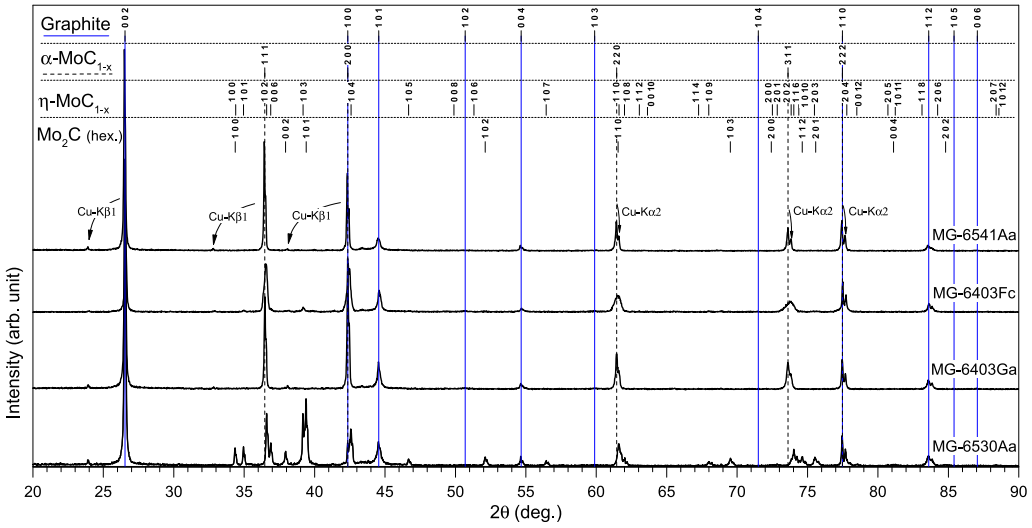

Fig. 10. XRD comparison of the four MoGr grades. (A colour version of this figure can be viewed online.)

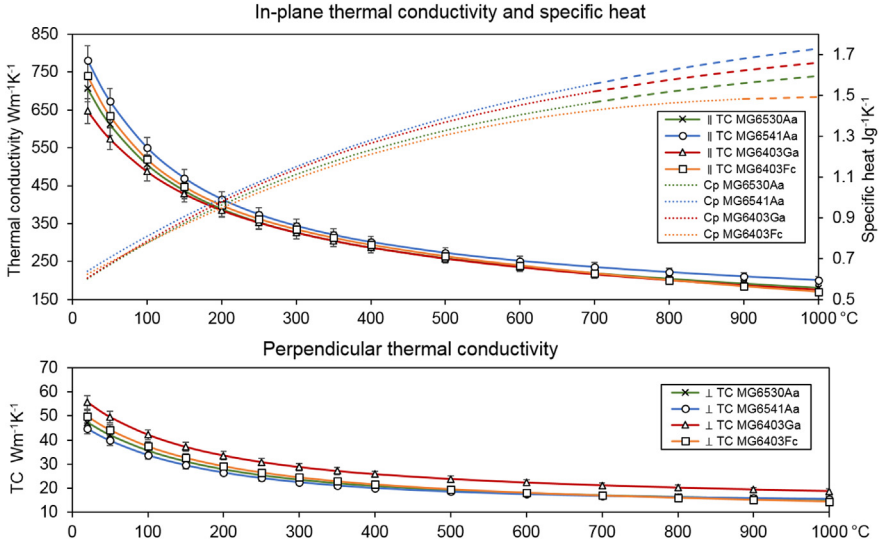

Fig. 11. (a) In-plane thermal conductivity and specific heat. Dashed line represents extrapolated specific heat curve. (b) Perpendicular thermal conductivity. (A colour version of this figure can be viewed online.)

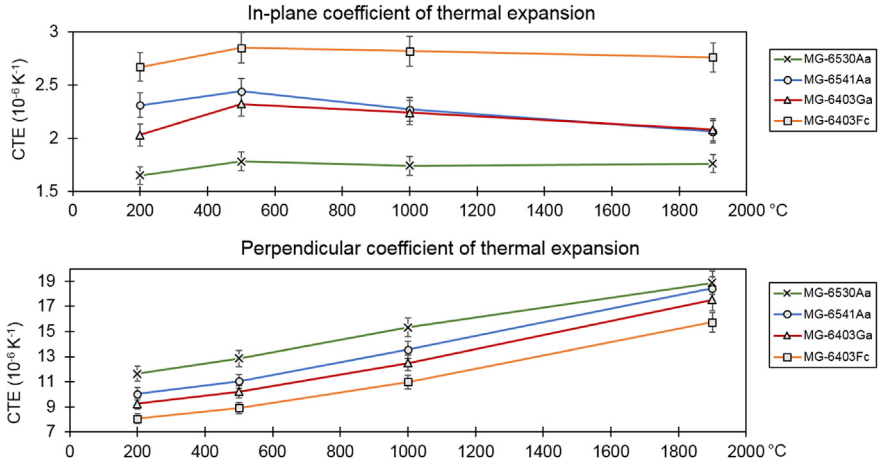

Fig. 12. Secant coefficients of thermal expansion 20–200°C, 20–500°C, 20–1000°C and 20–1900°C. The values shown are taken from the cooling-down ramp of the measurement. (A colour version of this figure can be viewed online.)

the high temperatures involved in the measurement. The behaviour under oxygen atmosphere has not been characterized yet, but it is expected to be comparable to graphite, as it is the main component of the composite.

3.4. Machinability

Since the material is mainly composed of graphite, it can easily be machined with conventional milling tools, in spite of the limited content of hard molybdenum carbides, similarly to other graphitic materials. Dry machining is adopted to assure ultra-high vacuum compatibility; a suction system equipped with filters collects the airborne dust generated during milling. Fig. 13a shows some of the MoGr blocks machined for a full-size collimator test. The blocks, which include features such as functional M8 threaded holes, chamfers or curved surfaces, are machined with a CNC milling machine. Small specimens for mechanical characterization have also been successfully produced (Fig. 13b).

4. Discussion

4.1. Carbon fibres

Carbon fibres (CF) were added with the purpose of improving the mechanical strength. Some influence in the thermal properties could also be expected due to the highly ordered nature of the pitch-based CFs.

Careful Scanning Electron Microscopy (SEM) examination of the fracture surfaces of bending test specimens revealed no visible trace of CFs. The diameter of the CFs ($10\,\mu m$) is probably small enough to be dissolved and re-precipitated by the molten Mo-C phase. A similar effect was observed but in solid nickel at $1100^{\circ}C$ in Ref. [42], where the dissolution-reprecipitation mechanism managed to completely dissolve and recrystallize CFs. In early MoGr grades, which were processed below the eutectic temperature, the CFs were not dissolved and were clearly visible in the microstructural examinations as bundles of agglomerated CFs [24].

The strengthening effect of the CFs on the mechanical properties is not demonstrated in this study; on the other hand, short CFs seem to have a beneficial role on thermo-physical properties (grade MG-6541Aa).

4.2. Titanium

The undoped molybdenum carbides, formed upon solidification of the eutectic mixture, experience three changes of phase until complete cool-down at RT, as shown in the Mo-C binary diagram (Fig. 5). The phase changes occurring at 1190 and $1655^{\circ}C$ in the binary system are detectable in the dilatometer measurements of perpendicular CTE, only in grade MG-6530Aa (without Ti), due to the change in density of the carbide phases, see Fig. 14. The phase changes are not visible in the in-plane measurements, either because of the texture of the carbide phases in the material or simply because the measured CTE is lower, leading to lower sensitivity to small variations of length.

The FCC carbides of molybdenum ($\alpha - MoC_{1-x}$) and titanium (TiC) exhibit completely solid solubility between them, resulting in a carbide phase $(Ti_{1-x}, Mo_x)_{1-y}C_y$, labelled δ in the ternary diagram, which is stable over a wide range of temperatures and stoichiometries [43], see Fig. 15. The effect of small quantities of titanium in MoGr, around one titanium atom every 9 molybdenum atoms, appears to be sufficient to turn all molybdenum carbide into the FCC phase ($\alpha - MoC_{1-x}$), over the full range of temperatures of interest.

XRD analyses performed in grades with titanium revealed the absence of hexagonal or orthorhombic molybdenum carbides and the presence of a FCC phase, with $a = 4.264$ Å, except a trace amount of $\eta - MoC_{1-x}$ in grade MG-6403Fc, probably due to the change in thermal treatment. According to the phase diagram Mo-C (Fig. 5), the cubic $\alpha - MoC_{1-x}$ phase is stable only above $1960^{\circ}C$, thus it is being stabilized down to RT with the Ti addition.

The absence of phase changes in the material is believed to be beneficial during beam impact scenarios, which could locally raise the temperature of collimator absorber materials to thousands of degrees. The presence of strongly stabilized phases usually improves the radiation resistance.

Despite the eutectic in equilibrium with carbon (graphite) moving from $2584^{\circ}C$ in Mo-C system ($45at.\%\,C$) to $2777^{\circ}C$ in Ti-C system ($65at.\%\,C$) (Fig. 15, points e_2 and e_1), the small addition of titanium should negligibly raise the eutectic temperature. In fact, a relevant difference in the melting temperature of the carbides was not observed with the sintering system used. The hot pressing strain seems to occur at a faster speed in the grades with Ti, which

Fig. 13. (a) MG-6530Aa machined blocks for full-size collimator test. External dimensions of the parts shown are 150 x 100 x 25 mm or 125 x 45 x 25 mm. (b) MG-6541Aa specimens for dynamic tests machined by Brevetti Bizz. Length is 30 mm and threads are M6.

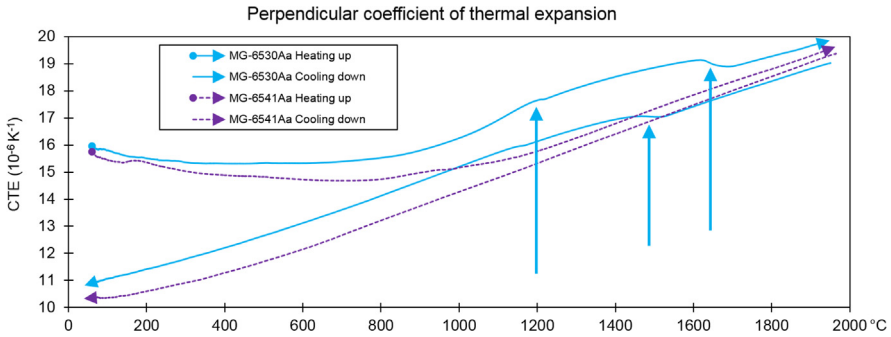

Fig. 14. Dilatometry test of MoGr without Ti addition (MG-6530Aa) and with Ti (MG-6541Aa), perpendicular-to-graphite-planes direction. Visible changes of volume due to phase transitions at 1190 °C, at 1655°*C* (heating) and at ∼ 1475°*C* (cooling). The behaviour shown is very repeatable in all samples of the same grade. (A colour version of this figure can be viewed online.)

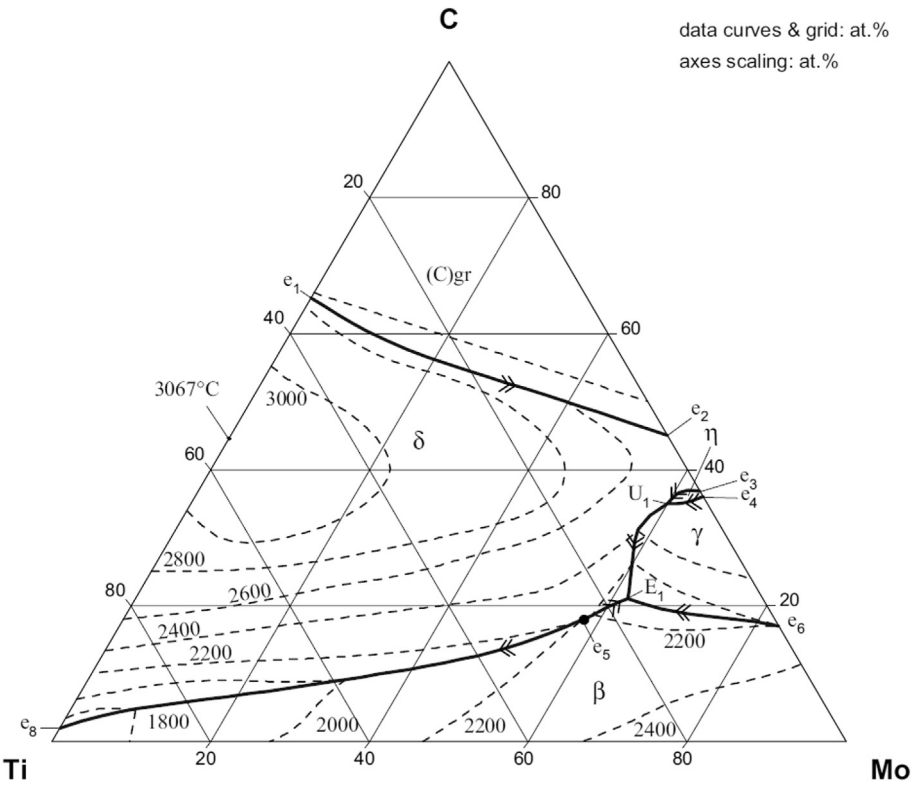

Fig. 15. Liquidus surface projection. C-Mo-Ti system [43]. Reprinted with permission.

could be related with a better mobility of the LP Mo-Ti-C. The higher affinity of Ti for carbon with respect to Mo, as seen in the standard enthalpies of formation of the carbides (*TiC* − 231, Mo_2C −46 and *MoC* −10 *kJ mol*$^{-1}$ [41]), could accelerate the catalytic graphitization process. Another difference observed is that the grades doped with Ti behave during machining as a harder material.

4.3. Processing temperature and outgassing behaviour

Collimators must operate in ultra-high vacuum (down to 10^{-10} *mbar*) to avoid undesired collisions between beam particles and gas molecules. This level of vacuum requires that collimator materials have outgassing rates lower than 10^{-12} *mbar l s*$^{-1}$*cm*$^{-2}$ at RT. Several MoGr grades produced exhibit outgassing rates 1 to 2 orders of magnitude above the specification, with gases from air as predominant species. Two sources are considered: the final surface of the blocks and gas trapped in the bulk. Concerning the former, tests are pointing to possible detrimental effects of the machining creating superficial micro-defects prone to gas trapping: this could be mitigated by applying surface treatments after production. As to the latter, special compaction techniques of the powders, changes in the sintering cycle and different thermal treatments under vacuum are being investigated.

To improve the outgassing behaviour, the temperature of the post-sintering cycle was increased in the grade MG-6403Fc in order to exceed again the eutectic point, to help the diffusion and outgassing of gas trapped inside the material, possibly coming from the first stages of pressing.

The higher post-sintering treatment temperature of grade MG-6403Fc increased the thermal expansion coefficient in the in-plane direction and decreased it in the perpendicular direction, pointing

to a higher degree of isotropy. The fact that the electrical conductivity is similar in grades MG-6403Ga and MG-6403Fc, while the strength in the latter slightly decreases (~ 20%), should be further investigated. A possible explanation is that the post-sintering treatment produces micro-cracks by relaxing internal stresses without breaking the conduction path.

The re-melting of the carbide inclusions in a pressure-free state in grade MG-6403Fc, is certainly releasing internal stresses, and it could also help to orient some graphite crystallites in a more efficient arrangement for an improved thermal conductance.

The reason of the excessive outgassing rates observed is not yet clear and intensive investigations are being performed to address the issue.

5. Conclusions

A family of graphite-matrix composite materials containing molybdenum carbide particles (MoGr), has been successfully developed for CERN future HL-LHC collimators. It is produced by spark plasma sintering assisted by molten metal-carbon liquid phase. The production parameters and the underlying physical mechanisms – such as catalytic graphitization – have been studied. An extensive characterization campaign has been performed; results have been presented for several of the grades produced. Microstructural and phase analysis have been performed.

As it is mainly composed of oriented graphite, the material exhibits a transversely isotropic behaviour with in-plane properties comparable to those of pure ordered graphites. However, unlike the latter, MoGr keeps reasonable thermo-physical and mechanical properties also in the direction perpendicular to the basal planes, making it in an attractive structural material for thermal management applications.

Small additions of titanium stabilize the FCC $\alpha - MoC_{1-x}$ phase down to room temperature. Ultrasonic bath cleaning has been found to modify the surface by removal of some graphite particles, this effect being more acute in surfaces parallel to graphite-basal planes. Carbon fibres seem to be dissolved and reprecipitated as graphite by the liquid phase; however effects on thermo-physical properties may still be attributed to their presence.

In the direction of graphite basal-planes, at room temperature, MoGr features a thermal conductivity approaching 800 $W\,m^{-1}K^{-1}$ and an electrical conductivity of around 1 $MS\,m^{-1}$. The coefficient of thermal expansion (secant) between room temperature and 200°C is in the order of $2.5 \times 10^{-6}\,K^{-1}$.

The thermal, electrical and mechanical properties of MoGr, combined with its low density ($2.5 - 2.6\,g\,cm^{-3}$), meet the requirements of collimators for the planned upgrade of CERN Large Hadron Collider (HL-LHC). However, the material grades presented in this paper exhibit air outgassing rates exceeding the specification for beam intercepting devices: this aspect is being addressed in order to fully satisfy ultra-high vacuum requirements and qualify the use of MoGr in particle accelerators.

The material can be produced in sizes compatible with industrial requirements and easily machined to the desired shape by conventional milling methods.

Besides high energy physics, the properties of molybdenum carbide - graphite composite make it appealing for a broad range of thermal management applications[4], particularly in aerospace and electronics, where reduced thermal expansion and low density are required along with high thermal conductivity or thermal shock resistance.

[4] Licensing opportunities for these materials can be discussed with CERN Knowledge Transfer (http://kt.cern/) or with Brevetti Bizz (www.brevettibizz.com)

Acknowledgements

The authors want to thank S. Redaelli, LHC collimation project leader, for the support given to this research. The authors wish to acknowledge the colleagues from the mechanical measurements lab at CERN for all the essential work carried out for this project: M. Guinchard, O. Sacristan-de-Frutos, L. Bianchi and E. Iakovakis; also the colleagues J. Busom-Descarrega, A.T. Perez-Fontenla and F. Leaux for the metallurgical support, and finally M. Tomut and P. Simon from GSI (Darmstadt, Germany) for many useful inputs and discussions. The research leading to these results has received funding from the European Commission under the FP7 Research Infrastructures project EuCARD-2, grant agreement No 312453. This project has received funding from the European Union's Horizon 2020 Research and Innovation programme under Grant Agreement No 730871. Research supported by the High Luminosity LHC project.

References

[1] E. Fermi, L. Szilard, US Patent 2,708,656, filing date December 19, 1944 (May 17 1955).
[2] O.S. Brüning, P. Collier, P. Lebrun, S. Myers, R. Ostojic, J. Poole, et al., LHC Design Report, CERN Yellow Reports: Monographs, CERN, Geneva, 2004, https://doi.org/10.5170/CERN-2004-003-V-1.
[3] A. Bertarelli, Beam-induced damage mechanisms and their calculation, CERN Yellow Reports 2 (0) (2016) 159, https://doi.org/10.5170/CERN-2016-002.159.
[4] A.W. Chao, Physics of Collective Beam Instabilities in High-energy Accelerators, Wiley-Interscience, 1993.
[5] A. Bertarelli, et al., The mechanical design for the LHC collimators, in: Proceedings, 9th European Particle Accelerator Conference (EPAC), Lucerne, Switzerland, 2004. https://cds.cern.ch/record/794628.
[6] A. Dallocchio, G. Belingardi, T. Kurtyka, A. Bertarelli, Study of Thermo-mechanical Effects Induced in Solids by High Energy Particle beams: analytical and Numerical Methods, Ph.D. thesis, Turin Polytechnic, 2008, https://cds.cern.ch/record/1314219.
[7] F. Carra, Thermomechanical Response of Advanced Materials under Quasi-instantaneous Heating, Ph.D. thesis, Turin Polytechnic, 2017.
[8] S. Redaelli, Beam cleaning and collimation systems, CERN Yellow Reports 2 (0) (2016) 403, https://doi.org/10.5170/CERN-2016-002.403.
[9] A. Bertarelli, E. Berthome, V. Boccone, F. Carra, F. Cerutti, N. Charitonidis, et al., An experiment to test advanced materials impacted by intense proton pulses at CERN HiRadMat facility, Nucl. Instrum. Methods Phys. Res. Sect. B Beam Interact. Mater. Atoms 308 (2013) 88–99, https://doi.org/10.1016/j.nimb.2013.05.007.
[10] G. Apollinari, I. Béjar Alonso, O. Brüning, M. Lamont, L. Rossi, High-luminosity Large Hadron Collider (HL-LHC): Preliminary Design Report, CERN Yellow Reports: Monographs, CERN, Geneva, 2015, https://doi.org/10.5170/CERN-2015-005.
[11] M. Benedikt, F. Zimmermann, Towards future circular colliders, J. Kor. Phys. Soc. 69 (6) (2016) 893–902, https://doi.org/10.3938/jkps.69.893.
[12] E. Metral, Beam Intensity Limitations, HiLumi LHC FP7 High Luminosity Large Hadron Collider Design Study Deliverable Report, CERN, Nov 2014. https://cds.cern.ch/record/1972601.
[13] M. Humenik, D. Hall, R.V. Alsten, Graphite-base cermets: a new material for bearing, electrical and high-temperature applications, Material Progress in Powder Metallurgy (1962) 101.
[14] J. White, J. Pontelandolfo, Graphite-carbide materials prepared by hot-working with the carbide phase in the liquid state, Nature 209 (1966) 1018–1019, https://doi.org/10.1038/2091018a0.
[15] J. White, J. Pontelandolfo, Graphite-carbide materials prepared by hot-working with a dispersed liquid-carbide phase, Carbon 4 (3) (1966) 305–314, https://doi.org/10.1016/0008-6223(66)90043-1.
[16] D. John, G.M. Jenkins, Hot-working and strengthening in metal carbide-graphite composites, J. Mater. Sci. 21 (8) (1986) 2941–2958, https://doi.org/10.1007/BF00551515.
[17] R. Matthews, Deformation and Strengthening in Molybdenum Carbide - Natural Graphite Composite Materials, Ph.D. thesis, University of Wales, 1970.
[18] R.B. Matthews, G.M. Jenkins, The high temperature interaction between molybdenum and graphite, J. Mater. Sci. 10 (11) (1975) 1976–1990, https://doi.org/10.1007/BF00754489.
[19] H.L. Riley, Amorphous carbon and graphite, Q. Rev. Chem. Soc. 1 (1947) 59–72, https://doi.org/10.1039/QR9470100059.
[20] A. Ōya, H. Marsh, Phenomena of catalytic graphitization, J. Mater. Sci. 17 (2) (1982) 309–322, https://doi.org/10.1007/BF00591464.
[21] P. Ouzilleau, A.E. Gheribi, P. Chartrand, The graphitization temperature threshold analyzed through a second-order structural transformation, Carbon 109 (2016) 896–908, https://doi.org/10.1016/j.carbon.2016.08.041.
[22] H.O. Pierson, Handbook of Carbon, Graphite, Diamonds and Fullerenes, Noyes

Publications, 1993.
[23] A. Bertarelli , S. Bizzaro, Inventors; CERN - European Organization For Nuclear Research, Brevetti Bizz S.R.L., assignees. A Molybdenum Carbide / Carbon Composite And Manufacturing Method, Int. Pat. Appl. (2013). PCT/EP2013/072818.
[24] N. Mariani, Development of Novel, Advanced Molybdenum-based Composites for High Energy Physics Applications, Ph.D. thesis, Milan Polytechnic, 2014, https://cds.cern.ch/record/2133098.
[25] I. Efthymiopoulos, C. Hessler, H. Gaillard, D. Grenier, M. Meddahi, P. Trilhe, et al., HiRadMat: a new irradiation facility for material testing at CERN, in: Proceedings, 2nd International Particle Accelerator Conference (IPAC), San Sebastian, Spain, 2011. https://cds.cern.ch/record/1403043.
[26] E. Quaranta, A. Bertarelli, N. Biancacci, R. Bruce, F. Carra, E. Métral, et al., Towards optimum material choices for the HL-LHC collimator upgrade, in: Proceedings, 7th International Particle Accelerator Conference (IPAC): Busan, Korea, 2016, https://doi.org/10.18429/JACoW-IPAC2016-WEPMW031.
[27] F. Carra, A. Bertarelli, A. Dallochio, L. Gentini, P. Gradassi, et al., Mechanical engineering and design of novel collimators for HL-LHC, in: Proceedings, 5th International Particle Accelerator Conference (IPAC): Dresden, Germany, 2014. https://cds.cern.ch/record/1748367.
[28] T. Noda, Graphitization of carbon under high pressure, Carbon 6 (2) (1968) 125–133, https://doi.org/10.1016/0008-6223(68)90297-2.
[29] B. Predel, C-Mo (Carbon-Molybdenum): datasheet from Landolt-Börnstein - group IV physical chemistry • volume 5B: "B-Ba – C-Zr", in: SpringerMaterials, 1992, https://doi.org/10.1007/10040476_643.
[30] L. Bianchi, Thermophysical and Mechanical Characterization of Advanced Materials for the LHC Collimation System, Master's thesis, Università de Pisa, 2017, https://cds.cern.ch/record/2265824.
[31] O. Sacristan-de-Frutos, A. Bertarelli, L. Bianchi, F. Carra, et al., Thermo-physical and mechanical characterisation of novel materials under development for HL-LHC beam intercepting devices, in: Proceedings, 8th International Particle Accelerator Conference (IPAC) Copenhagen, Denmark, 2017, https://doi.org/10.18429/JACoW-IPAC2017-WEPVA113.
[32] E. Iakovakis, Thermophysical and Mechanical Characterization of Novel Advanced Materials for the LHC Collimation System, Master's thesis, Aristotle University of Thessaloniki, 2015.
[33] M. Borg, Numerical Modelling and Experimental Testing of Novel Materials for LHC Collimators, Master's thesis, University of Malta, 2015.
[34] C. Suryanarayana, M. Grant Norton, X-Ray Diffraction. A Practical Approach, Springer, 1998.
[35] J.Y. Howe, C.J. Rawn, L.E. Jones, H. Ow, Improved crystallographic data for graphite, Powder Diffr. 18 (2) (2003) 150–154, https://doi.org/10.1154/1.1536926.
[36] J. Dubois, T. Epicier, C. Esnouf, G. Fantozzi, P. Convert, Neutron powder diffraction studies of transition metal hemicarbides M_2C_{1-x} – I. motivation for a study on W_2C and Mo_2C and experimental background for an in situ investigation at elevated temperature, Acta Metall. 36 (8) (1988) 1891–1901, https://doi.org/10.1016/0001-6160(88)90292-1.
[37] T. Epicier, J. Dubois, C. Esnouf, G. Fantozzi, P. Convert, Neutron powder diffraction studies of transition metal hemicarbides M_2C_{1-x} – II. in situ high temperature study on W_2C_{1-x} and Mo_2C_{1-x}, Acta Metall. 36 (8) (1988) 1903–1921, https://doi.org/10.1016/0001-6160(88)90293-3.
[38] E. Parthé, V. Sadagopan, The structure of dimolybdenum carbide by neutron diffraction technique, Acta Crystallogr. 16 (3) (1963) 202–205, https://doi.org/10.1107/S0365110X63000487.
[39] H. Nowotny, Alloy chemistry of transition element borides, carbides, nitrides, aluminides, and silicides, in: Electronic Structure and Alloy Chemistry of the Transition Elements, Wiley (Interscience), 1963.
[40] H.O. Pierson, Handbook of Refractory Carbides and Nitrides: Properties, Characteristics, Processing and Applications, Noyes Publications, Park Ridge, NJ, 1996.
[41] G. Samsonov, I. M. Vinitskii, Handbook of Refractory Compounds, IFI/Plenum, 1980 (translated from Russian by Kenneth Shaw).
[42] P.W. Jackson, J.R. Marjoram, Compatibility studies of carbon fibres with nickel and cobalt, J. Mater. Sci. 5 (1) (1970) 9–23, https://doi.org/10.1007/BF02427179.
[43] A. Kroupa, A. Watson, Carbon-molybdenum-titanium. Landolt-börnstein - Group IV Physical Chemistry 11E2 (Refractory Metal Systems), copyright 2010 Springer-Verlag Berlin Heidelberg, 2010, https://doi.org/10.1007/978-3-642-02700-0_31.